coatings

MDPI

Article

Homogeneous Self-Assembled Monolayers Fabricated in Ambient Conditions via Solvent Engineering for Inverted Perovskite Solar Cells

Xinkang Su, Guoxin Shi, Longhao Li, Cuncun Wu, Yangyang Zhang and Fangzhou Liu *

Tianjin Key Laboratory of Materials Laminating Fabrication and Interface Control Technology, School of Materials Science and Engineering, Hebei University of Technology, Tianjin 300401, China
* Correspondence: liufz@hebut.edu.cn

Highlights

What are the main findings?

- This work firstly confirms that ambient humidity remarkably affects the inhomogeneous aggregation of self-assembled monolayers (SAMs).
- Protic polar solvents cause severe aggregation of SAMs under ambient conditions, while aprotic polar solvents alleviate this defect.
- The ethanol (EtOH)/N,N-dimethylformamide (DMF) mixed-solvent system enables the fabrication of uniform SAM films and improves interfacial properties.

What are the implications of the main findings?

- Uniform SAM films can be fabricated under humid ambient conditions, which simplifies device preparation conditions.
- This work provides a feasible ambient fabrication strategy for the industrialization of perovskite solar cells.
- The solvent engineering offers references for preparing similar self-assembled monolayer systems in ambient air.

Abstract

Benefiting from the booming development of self-assembled monolayer (SAM) based hole-transporting materials, inverted perovskite solar cells (PSCs) have attained a certified power conversion efficiency (PCE) beyond 27.0%, exhibiting great potential for commercialization. However, conventional SAM molecules are prone to self-aggregation owing to their inherent molecular configurations, which readily induced defective and inhomogeneous deposition. In addition, state-of-the-art SAM-based hole-transporting layers are generally deposited in inert environments, while the ambient moisture is expected to further deteriorate the homogeneity of the SAM layers. In this work, a mixed-solvent system of ethanol/N,N-dimethylformamide (DMF) was adopted for the deposition of Me-4PACz SAMs in ambient conditions, which enables significant suppression of intermolecular aggregation in precursor solution and moisture-induced inhomogeneity. The high-quality homogeneous SAM-based hole-transporting layers, along with subsequently optimized perovskite buried interface properties, further empower a prominent increase in the PCE of inverted PSC devices up to 25.0%.

Keywords: perovskite solar cells; self-assembled monolayer; ambient humidity; solvent engineering

Academic Editor: Alessandro Latini

Received: 11 June 2026
Revised: 27 June 2026
Accepted: 30 June 2026
Published: 11 July 2026

1. Introduction

Inverted p-i-n perovskite solar cells (PSCs) have attracted extensive research attention owing to their outstanding stability, low fabrication cost and superior compatibility with tandem devices [1–3]. This device architecture was first reported by Jeng et al. in 2013 with a modest power conversion efficiency (PCE) of only 3.9% [4]. Ever since the establishment of the inverted PSC architecture, conductive polymers such as poly(3,4-ethylenedioxythiophene)-poly-(styrenesulfonate) (PEDOT:PSS) and poly-(triarylamine) (PTAA) have been successfully employed as viable materials for the hole-transporting layer (HTL) [5]. In 2018, the report on V1036-type self-assembled monolayer (SAM) based HTL opened up an alternative route toward high-performance inverted PSCs [6,7]. The rapid progress in the development of new SAM molecules such as [4-(2,7-dibromo-9,9-dimethylacridin-10(9H)-yl)butyl]phosphonic acid (DMAcPA) has led to a boost in the photovoltaic performance of inverted PSCs [8]. To date, inverted PSCs adopting SAM-based HTLs have surpassed the efficiency threshold of 27%, highlighting the great application potential of SAM materials [9]. Compared with the conventional polymeric and inorganic oxide hole transporting materials, SAM molecules can anchor onto the surfaces of the transparent conducting oxide (TCO) substrates via the dissociative chemisorption between the anchoring groups and the surface O-H bond, and form π–π stacking interactions between carbazole moieties of adjacent molecules, thereby forming a vertically aligned and structurally robust monolayer [10]. Benefiting from the unique self-assembly feature and favorable energy-level alignment, SAMs exhibited excellent hole-extraction capability [11,12].

Scalable and repeatable fabrication of SAM-based HTLs remains a critical bottleneck for the industrialization of inverted PSCs. The interfacial properties of SAM layers directly govern hole extraction and transportation, while also modulating the morphology, crystallization and optoelectronic properties of the overlying perovskite layers [13–15]. The overlapping of delocalized π-electron clouds among aromatic rings can generate weak noncovalent attraction, driving SAM molecules to stack in parallel, slipped or face-to-face configurations and thus form ordered or disordered aggregates [16,17]. Due to inherent molecular structures, SAM molecules tend to spontaneously aggregate in precursor solutions, resulting in inhomogeneous SAM deposition. Such undesired self-aggregation and the consequently inhomogeneous SAM deposition would potentially deteriorate device performance [18,19]. Several strategies have been reported to tackle this pivotal challenge limiting further advances of inverted PSCs. Liu et al. proposed an IPA/DMF cosolvent system to dissociate carbazole-based molecular micelles [20], activate phosphonic acid anchoring groups and facilitate the formation of compact and uniform SAM layers on substrates; devices fabricated via this strategy achieved a PCE of 25.0% [21].

Nevertheless, in addition to the spontaneous intermolecular aggregation, scalability of SAM-based HTLs is significantly limited by the stringent environmental requirement for deposition processes. In most published works on highly efficient inverted PSCs, the deposition of SAM-based HTLs was generally carried out in an inert environment, for instance, nitrogen-filled gloveboxes, with rigorous moisture exclusion during precursor solutions and film preparation [22,23]. Moreover, nearly all reported modulation approaches were confined to inert atmospheres [24]. Such strict demand for an inert fabrication environment has inevitably hindered upscaling and large-area manufacturing of SAM-based HTLs for commercialization of inverted PSCs. To expand the fabrication in ambient conditions, moisture becomes a significant factor affecting the quality of SAM layers. Nevertheless, systematic investigations focusing on the influence of moisture on SAM deposition and the corresponding optimization strategies remain insufficient.

Against this backdrop, this work is targeted to achieve homogeneous deposition of SAM layers in ambient conditions via solvent engineering. Common solvents, based on their polarity and protic/aprotic properties, were systematically evaluated for their capability of dissolving the SAM molecules while suppressing intermolecular aggregation. A mixed-solvent system was introduced to achieve an optimized SAM solution, where the intermolecular aggregation and the detrimental effect of ambient moisture are effectively alleviated. Accordingly, a homogeneous SAM-based HTL with an optimized surface energy landscape was successfully achieved in ambient conditions at 55% relative humidity (RH). As a proof of concept, inverted PSC devices with the optimized SAM-based HTL were fabricated, demonstrating a considerably increased PCE up to 25.0%. This work offers a feasible approach toward scalable fabrication of high-efficiency inverted PSCs in ambient conditions.

2. Materials and Methods

2.1. Materials

Formamidinium iodide (FAI, 99.90%) and lead iodide (PbI_2, 99.99%) were purchased from Advanced Electronic Technology Co., Ltd. (Dalian, China). Methylammonium chloride (MACl, 99.9%), 2,9-dimethyl-4,7-diphenyl-1,10-phenanthroline (BCP, 99.50%), piperazine dihydroiodide (PipDI, 99.5%), 2-[3-(trifluoromethyl)phenyl]ethan-1-aminium (CF_3-PEABr, 99.00%) and n-Hexane (n-Hex, 99.00%) were purchased from Yuri Solar Co., Ltd. (Xi'an, China). [4-(3,6-dimethyl-9H-carbazol-9-yl) butyl] phosphonic acid (Me-4PACz, 99.00%) was purchased from TCI (Tokyo, Japan). Sodium 4-chlorobenzenesulfonate (4Cl-BZS, 98.00%) was purchased from Macklin (Shanghai, China). [6,6]-Phenyl C_{61} butyric acid methyl ester ($PC_{61}BM$, 99.80%) was purchased from Lumtec (New Taipei, Taiwan). Ethanol (EtOH, 99.80%) and ethyl acetate (EA, 99.80%) were purchased from Aladdin (Shanghai, China). N,N-dimethylformamide (DMF, 99.80%), N-methylpyrrolidone (NMP, 99.50%), methanol (MeOH, 99.90%) and isopropanol (IPA, 99.90%) were purchased from InnoChem (Beijing, China). Chlorobenzene (CB, 99.90%) and dimethyl sulfoxide (DMSO, 99.90%) were purchased from Thermo Scientific (Waltham, MA, USA). All the chemicals were used as received without further purification.

2.2. Experimental Methods

ITO substrates (2 × 2 cm^2) were cleaned by sequential ultrasonication in detergent solution, deionized water and ethanol for 30 min, respectively. The cleaned ITO-coated glass substrates were then dried with nitrogen. Before use, the substrates were subjected to UV-ozone treatment for 20 min. For the preparation of SAM solutions, Me-4PACz was dissolved in selected solvents at a concentration of 0.5 mg/mL. SAM-based hole transport layer (HTL) was deposited under ambient conditions (25 ± 5 °C, 55% RH) by spin-coating the Me-4PACz solution at 4000 rpm for 30 s, followed by annealing at 115 °C for 10 min. For the Me-4PACz solutions adopting a mixed solvent system, Me-4PACz was dissolved in ethanol/DMF (volume ratio = 3:1) at a concentration of 0.5 mg/mL. The corresponding SAM-based HTLs were fabricated following the identical processing conditions described above.

The perovskite layer was deposited via a low-pressure-assisted (LPA) method. A 1.4 M $FAPbI_3$ perovskite precursor solution was prepared by dissolving stoichiometric FAI and PbI_2 in a mixed solvent of DMF/NMP (volume ratio = 9:1) with the addition of MACl (15 mol%) and 4Cl-BZS (1 mg/mL). The perovskite precursor solution was stirred for 2 h, and then spin-coated on the SAM-based HTLs at 4000 rpm for 8 s. The obtained wet film was immediately transferred into a vacuum chamber within 3 s and held in a low-pressure

environment (20 Pa) for 60 s to remove excess residual solvents. Afterwards, the film was annealed at 130 °C for 20 min in ambient.

For the surface passivation layer, CF_3-PEABr solution (0.3 mg/mL) and PipDI solution (0.3 mg/mL) dissolved in isopropyl alcohol were sequentially spin-coated on the as-prepared perovskite film at 5000 rpm for 30 s, followed by annealing at 100 °C for 5 min. For the deposition of the electron transport layer (ETL), a $PC_{61}BM$ solution (20 mg/mL in chlorobenzene) was spin-coated onto the perovskite film at 1200 rpm for 30 s. After that, a BCP solution (0.5 mg/mL in isopropanol) was spin-coated at 5000 rpm for 30 s. Finally, an 85 nm thick silver electrode was thermally evaporated through a shadow mask. The completed PSC devices have a p-i-n configuration of ITO/Me-4PACz/$FAPbI_3$/CF_3-PEABr/PipDI/$PC_{61}BM$/BCP/Ag with an active area of 0.038 cm^2.

2.3. Characterizations

Scanning electron microscopy (SEM) images were acquired with a Thermo Apreo 2S microscope (Thermo Scientific, Waltham, MA, USA) at an accelerating voltage of 3 kV. Atomic force microscopy (AFM) and Kelvin probe force microscopy (KPFM) analyses were performed using an Asylum MFP-3D Bio atomic force microscope (Oxford Instruments, High Wycombe, UK). Photoluminescence (PL) spectra were recorded on a NanoLog FL3-2Ihr fluorescence spectrometer (HORIBA Scientific, Kyoto, Japan) under 450 nm excitation. Time-resolved photoluminescence (TRPL) measurements were carried out using a Delta Flex ultrafast lifetime spectrometer (HORIBA Scientific, Kyoto, Japan). PL lifetime mapping was completed with an ISS Q2 laser confocal scanning multi-functional imaging system (ISS, Champaign, IL, USA). X-ray photoelectron spectroscopy (XPS) analyses of the as-prepared films were conducted on a PHI 5000 VersaProbe III system (ULVAC-PHI, Inc., Chigasaki, Japan).

Current density-voltage (*J-V*) curves of perovskite solar cell (PSC) devices were measured under simulated AM 1.5G solar irradiation (100 mW/cm^2) using an EASISOLAP-50-3A xenon lamp solar simulator (CROWNTECH, Inc., Macungie, PA, USA). A certified reference cell was used for light intensity calibration. Voltage scans were executed in the reverse direction (1.2 V to −0.1 V) and forward direction (−0.1 V to 1.2 V) with a Keithley 2400 SourceMeter (Tektronix, Inc., Beaverton, OR, USA). External quantum efficiency (EQE) spectra were obtained using a QE-R quantum efficiency measurement system (Enli Technology, Kaohsiung, Taiwan). All characterizations were carried out on unencapsulated devices under ambient conditions at room temperature.

3. Results

3.1. Effect of Solvent Modulation on SAM Deposition

In this work, [4-(3,6-dimethyl-9H-carbazol-9-yl) butyl] phosphonic acid (Me-4PACz) was employed as the target SAM molecules to study the effect of intermolecular aggregation and ambient moisture on SAM deposition in ambient conditions. When SAM-based HTLs are deposited in ambient conditions with the presence of moisture, the combined effects of intermolecular aggregation and ambient moisture can induce obvious micron-scale aggregates and inhomogeneous film morphology. Solvent modulation was therefore adopted as an effective approach to suppress the spontaneous aggregation of SAM molecules. First, common solvents are categorized based on their polarity and protic/aprotic properties, and three representative solvents from each category are selected to investigate their feasibility for dissolving SAM molecules (Figure 1). The molecular structures of the selected solvents, namely protic polar solvents (EtOH, MeOH, IPA), aprotic polar solvents (DMF, NMP, DMSO), and nonpolar solvents (CB, EA, n-Hex), are presented, and their key physicochemical properties, such as polarity and boiling point, are summarized in Table 1 [25,26]. These

key factors are expected to largely determine the dissolution, dispersion and deposition behaviors of the target SAM molecules.

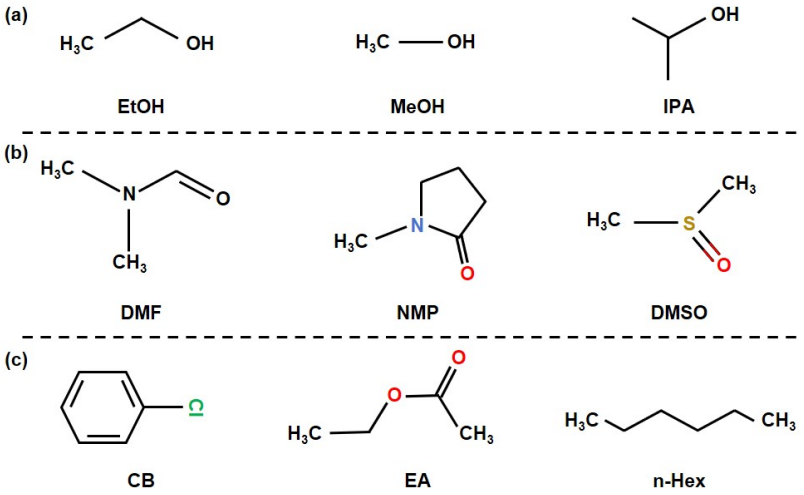

Figure 1. Molecular structures of common solvents selected for investigation based on their polarity and protic/aprotic properties. (**a**) protic polar solvents EtOH, MeOH and IPA; (**b**) aprotic polar solvents DMF, NMP and DMSO; (**c**) nonpolar solvents CB, EA and n-Hex.

Table 1. Key physicochemical parameters of the solvents selected for investigation in this work.

Solvents	Viscosity (mPa·s)	Permittivity	Dipole Moment (D)	Boiling Point (°C)
EtOH	1.074	24.50	1.69	78.4
MeOH	0.544	32.60	1.70	64.7
IPA	2.050	18.30	4.66	82.4
DMF	0.920	38.30	3.86	153.0
NMP	1.650	32.00	4.09	202.0
DMSO	2.000	46.70	3.96	189.0
CB	0.564	5.69	1.69	131.7
EA	0.450	6.02	1.78	77.1
n-Hex	0.307	1.88	0.07	68.7

Me-4PACz solutions with selected solvents were prepared and deposited on the ITO surface in ambient conditions (55% RH). The SEM images of the obtained SAM layers are shown in Figure 2, where sharp distinctions in the film morphology and aggregation behaviors can be observed among different samples. The morphological modulation of SAM films by different solvents has been reported to stem from the synergistic effects of solvation capacity, evaporation rate and interfacial interactions [27,28]. Protic polar solvents (EtOH, MeOH, IPA) exhibit weak coordination with SAM molecules and therefore cannot disassemble intermolecular aggregation in precursor solutions. During the spin-coating and the subsequent annealing process for rapid removal of solvent, moisture adsorbed on ITO substrates may compete with SAM molecules for available anchoring sites, which likely exacerbates the inhomogeneity of the obtained SAM layer. Among the selected protic solvents, EtOH and MeOH have low boiling points, and the corresponding SAM films exhibit micrometer-scale aggregated domains (Figure 2a,b). In contrast, IPA exhibits lower polarity and a higher boiling point, which may lead to the formation of smaller but densely distributed aggregates in the corresponding SAM layer (Figure 2c). In general, all SAM layers deposited with the selected protic solvents exhibit severe morphology inhomogeneity.

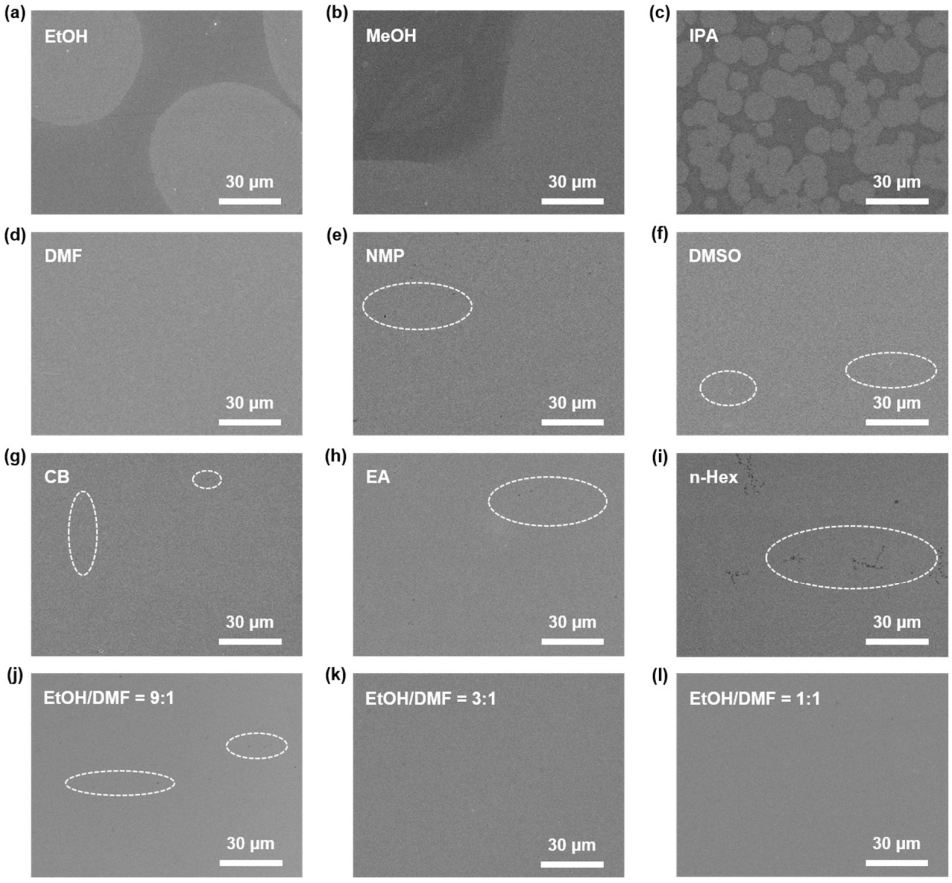

Figure 2. SEM images of SAM-based HTL deposited in ambient conditions with different solvents: (**a**) EtOH; (**b**) MeOH; (**c**) IPA; (**d**) DMF, (**e**) NMP; (**f**) DMSO; (**g**) CB; (**h**) EA; (**i**) n-Hex; (**j**) EtOH:DMF = 9:1; (**k**) EtOH:DMF = 3:1; (**l**) EtOH:DMF = 1:1.

On the other hand, aprotic polar solvents (DMF, NMP, DMSO) can enhance the dispersion of Me-4PACz through strong dipole–dipole interactions and coordination effects [29]. Their relatively high boiling points enable slow and controllable solvent evaporation while inhibiting the adsorption of moisture on the ITO surface, thus relieving moisture-triggered aggregation and precipitation during spin-coating. The gradual volatilization of the solvent during annealing can also facilitate ordered rearrangement of SAM molecules. Among the selected aprotic polar solvents, DMSO shows strong coordination capability, while NMP has the highest boiling point, which is favorable to stabilizing Me-4PACz dispersion in the precursor solutions. All three aprotic solvents generally lead to the formation of smooth and homogeneous SAM coatings except for a few discernible morphological flaws (areas in dotted circle, Figure 2d–f).

Finally, nonpolar solvents (CB, EA, n-Hex) exhibit low solubility of Me-4PACz, which results in rapid precipitation and anchoring of SAM molecules on the ITO surface during spin-coating and annealing. Owing to their weak polarity, these solvents barely compete for anchoring sites with SAM molecules. In addition, the residual solvent can be completely removed after annealing at 115 °C without disrupting the ordered rearrangement of SAM molecules. Among the selected nonpolar solvents, CB has a moderate boiling point and polarity but is inherently toxic. EA has slightly higher polarity and better solubility for Me-4PACz, while n-Hex exhibits the weakest polarity and poorest solubility. In general, the selected nonpolar solvents can reduce competitive molecular adsorption on the ITO surface, thereby yielding relatively uniform SAM layers except for some nanoscale, discernible morphological flaws (areas in dotted circles, Figure 2g–i).

Among all the solvents investigated, N,N-dimethylformamide (DMF), featuring strong polarity and a low boiling point, was first considered as a suitable solvent since it can considerably optimize the dispersion of SAM molecules in the precursor solutions. Nevertheless, this aprotic polar solvent may also compete with SAM molecules for the available adsorption sites, which substantially hinders the adsorption and anchoring of SAM molecules on the ITO surface [28]. To address this issue, a mixed solvent system of EtOH/DMF was further adopted for the Me-4PACz solutions. As shown in Figure 2j,k, the SAM layers deposited with the EtOH/DMF solvent system retain a homogeneous morphology across a wide range of EtOH/DMF volume ratios, and the morphology is further improved with increased DMF proportion in the mixed solvent. To further study the profound influence of solvent engineering on the SAM layer properties, a representative EtOH/DMF volume ratio of 3:1 was used for the Me-4PACz samples prepared employing the mixed EtOH/DMF solvent system for the subsequent characterizations. For clarity, the SAM layers deposited with the mixed solvent system are denoted as EtOH/DMF samples, while the SAM layers deposited with conventional ethanol solvent are used as the reference group and referred to as EtOH samples in the later discussion.

The surface potential of the SAM layers adopting different solvents is characterized using Kelvin probe force microscopy (KPFM), as shown in Figure 3a,b. The surface potential of the EtOH sample exhibits a bimodal distribution within the range from −400 mV to −340 mV, manifesting remarkably inhomogeneous SAM deposition. On the contrary, the EtOH/DMF mixed solvent system can effectively ameliorate the film uniformity, evidenced by a unimodal distribution of surface potential centered around −370 mV (Figure 3d,e). XPS analysis was employed to evaluate the chemical environment of the SAM layers. The O 1s XPS core spectra of EtOH and EtOH/DMF samples are shown in Figures 3c and 3f, respectively [30]. The relative area of the signal corresponding to -OH peaks derived from the bonding between phosphonic acid moieties of SAM molecules and the ITO surface (532.2 eV) has increased from 16.07% to 18.97% upon adopting the mixed solvent system. Such observation verifies the considerably enhanced anchoring of the SAM molecules on the ITO surface.

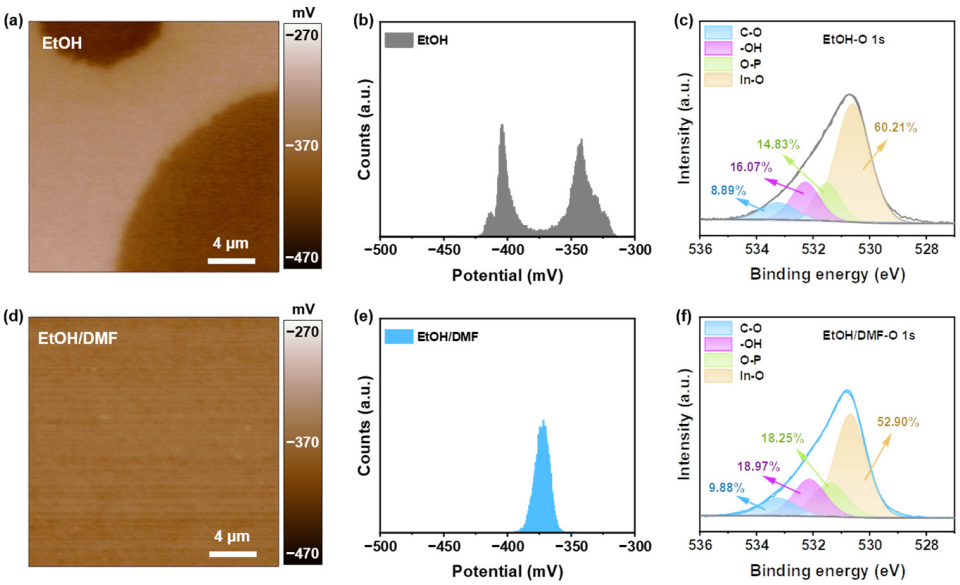

Figure 3. (**a**) KPFM surface potential mapping and (**b**) the corresponding histogram of the EtOH sample; (**c**) Fitted O 1s XPS spectra of the EtOH sample; (**d**) KPFM surface potential mapping and (**e**) the corresponding histogram of the EtOH/DMF sample; (**f**) Fitted O 1s XPS spectra of the EtOH/DMF sample.

3.2. Effect of Solvent Engineering on Perovskite Buried Interface

$FAPbI_3$ perovskite films were deposited on the SAM layers adopting different solvent systems, and the obtained perovskite samples are denoted accordingly as EtOH and EtOH/DMF samples. To investigate the subtle influence of SAM layer quality on the overlying perovskite layer and the carrier dynamics at the perovskite/HTL interface, the perovskite films were delaminated from the substrate using a UV-curable epoxy following a previously reported work [31], so that the buried interface properties can be directly assessed. SEM images of the perovskite buried interfaces are shown in Figure 4a,d, where the EtOH/DMF sample exhibits remarkably reduced pinholes and relatively larger grain sizes compared to the EtOH sample. KPFM characterization was performed to probe the surface potential of the buried interface within a scanning area of 5×5 μm^2 [32]. The EtOH/DMF sample exhibits a more homogeneous surface potential distribution from 60 mV to 160 mV (Figure 4e,f), in marked contrast to the multipeak distribution from 40 mV to 160 mV for the EtOH sample (Figure 4b,c). These results demonstrate that the SAM layer quality has a prominent influence on the morphology and surface potential of the perovskite buried interface. A high-quality, homogeneous SAM layer can ultimately lead to reduced structural defects and more uniform surface potential distribution at the buried interface, which is beneficial to the interfacial charge extraction and transport.

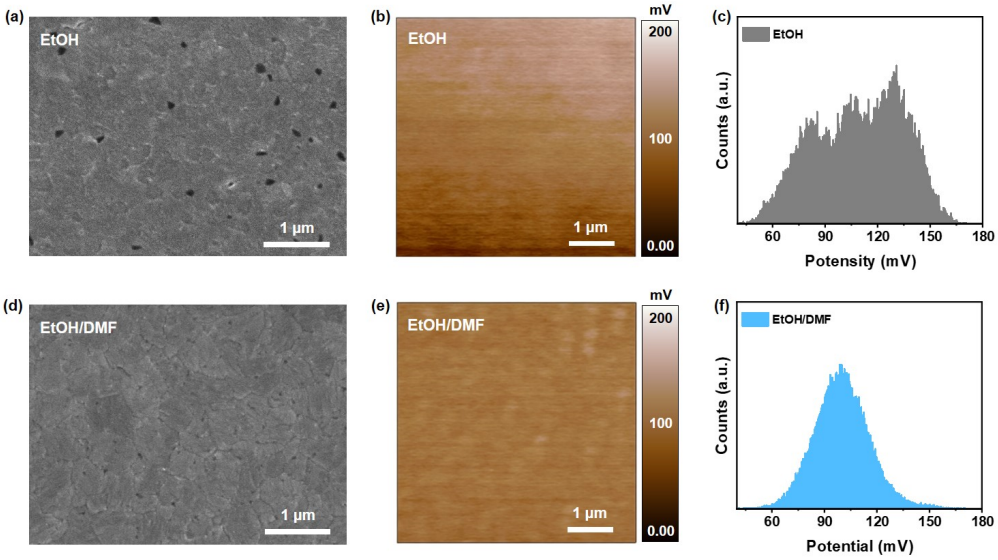

Figure 4. (**a**) SEM image of the buried interface of EtOH sample; (**b**) KPFM surface potential mapping and (**c**) the corresponding histogram of the buried interface of EtOH sample; (**d**) SEM image of the buried interface of EtOH/DMF sample; (**e**) KPFM surface potential mapping and (**f**) the corresponding histogram of the buried interface of EtOH/DMF sample.

PL intensity and lifetime characterization are conducted at the perovskite buried interface to evaluate the interface optoelectronic properties, as shown in Figure 5 [33]. In general, the EtOH/DMF sample exhibits enhanced PL intensity and extended carrier lifetime compared to the EtOH sample. The time-resolved PL (TRPL) spectra in Figure 5f are further fitted using a bi-exponential model:

$$I_{\mathrm{TRPL}}(t) = A_1 e^{-t/\tau_1} + A_2 e^{-t/\tau_2}, \quad (1)$$

where the two exponential decay components in the equation are generally assigned to the trap-related recombination featuring a shorter lifetime and the radiative recombination with a longer lifetime, respectively [34]. Table 2 summarizes the amplitude (A_1, A_2) and lifetime (τ_1, τ_2) of each component retrieved from the fitting. The EtOH/DMF sample

exhibits an extended average carrier lifetime of 1665.33 ns compared with 1174.39 ns for the EtOH sample, demonstrating significantly reduced defects and enhanced carrier dynamics at the perovskite/HTL interface [35].

Table 2. Fitting results of TRPL spectra of the EtOH and the EtOH/DMF samples obtained from a bi-exponential model. A_1 and τ_1 denote the relative amplitude and lifetime of the exponential decay component corresponding to the trap-related recombination, while A_2 and τ_2 denote the relative amplitude and lifetime of the exponential decay component attributed to the radiative recombination, respectively.

Sample	A_1 (%)	τ_1 (ns)	A_2 (%)	τ_2 (ns)	τ_{ave} (ns)
EtOH	1.18	176.58 ± 12.40	98.82	1176.18 ± 1.12	1174.39
EtOH/DMF	0.13	845.60 ± 13.16	99.87	1665.87 ± 2.86	1665.33

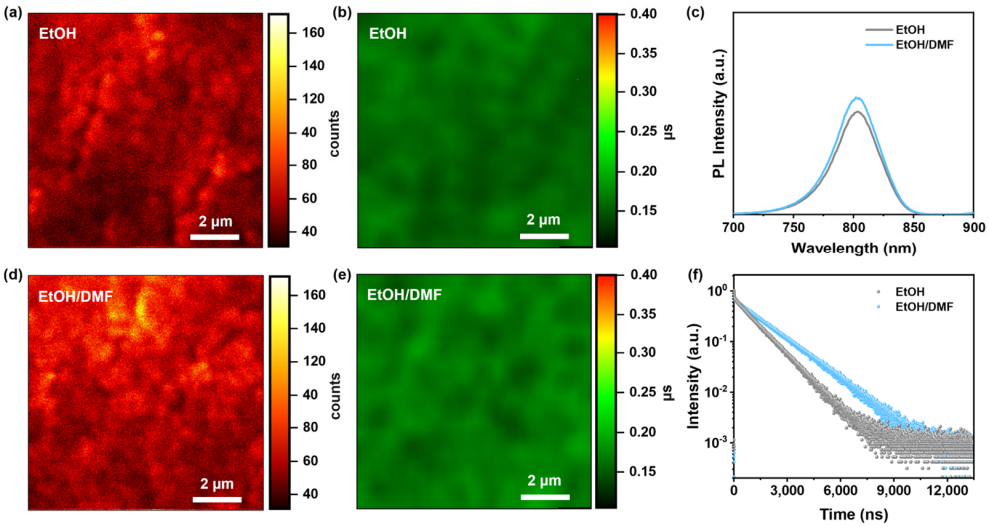

Figure 5. (**a**) PL intensity and (**b**) lifetime mapping at the perovskite buried interface of the EtOH sample; (**c**) steady-state PL spectra of the EtOH and the EtOH/DMF samples; (**d**) PL intensity and (**e**) lifetime mapping at the perovskite buried interface of the EtOH/DMF sample; (**f**) TRPL spectra of the EtOH and the EtOH/DMF samples.

3.3. Effect of Solvent Engineering on the PSC Device Performance

To probe the optimum volume ratio of the mixed solvent system for Me-4PACz solution, SAM layers adopting an EtOH/DMF mixed solvent system with different EtOH:DMF volume ratios are deposited in ambient conditions (55% RH). Subsequently, the corresponding inverted PSC devices were fabricated with the configuration of ITO/Me-4PACz/$FAPbI_3$/CF_3-PEABr/PipDI/PCBM/BCP/Ag. The *J-V* curves of the champion devices corresponding to different solvent conditions are plotted in Figure 6a, while their primary photovoltaic parameters are summarized in Table 3. The measurement results indicate that the PSC devices achieved an optimal PCE of 24.6% with an EtOH/DMF volume ratio of 3:1. By further optimizing the fabrication processes, the champion device delivers a PCE of 25.0% with a short-circuit current density (J_{SC}) of 25.52 mA/cm^2 and a fill factor (FF) of 82.90% (Figure 6b), which is remarkably improved compared with the device fabricated with conventional ethanol solution of Me-4PACz. The champion device also demonstrates a steady-state power output efficiency of 24.5% at 1.02 V bias voltage, while the device based on EtOH SAM layer showed a steady-state efficiency of 24.0% at 1.01 V (Figure 6c). External quantum efficiency (EQE) measurements were also performed for the EtOH and EtOH/DMF devices, as shown in Figure 6d. The integrated current density of the EtOH/DMF device was 24.50 mA/cm^2, which exceeded the value of 24.13 mA/cm^2 for

the EtOH device. In addition, the integrated current density of both EtOH and EtOH/DMF devices agrees well with the J_{SC} values obtained from *J-V* characteristics (4.62% and 3.99% mismatch, respectively) as summarized in Table 4.

Table 3. Primary photovoltaic parameters including the short-circuit current density (J_{SC}), open-circuit voltage (V_{OC}), fill factor (FF), and power conversion efficiency (PCE) of devices fabricated with SAM solutions at different EtOH/DMF volume ratios.

Sample	J_{SC} (mA/cm^2)	V_{OC} (V)	FF (%)	PCE (%)
EtOH	25.45	1.170	80.49	24.0
EtOH:DMF = 50:1	25.44	1.166	81.94	24.3
EtOH:DMF = 30:1	25.57	1.163	81.94	24.4
EtOH:DMF = 9:1	25.54	1.160	81.32	24.1
EtOH:DMF = 3:1	25.80	1.161	81.95	24.6
EtOH:DMF = 1:1	25.40	1.161	82.58	24.4
EtOH:DMF = 1:3	25.71	1.154	81.77	24.3

Table 4. Primary photovoltaic parameters including the short-circuit current density (J_{SC}), open-circuit voltage (V_{OC}), fill factor (FF), and power conversion efficiency (PCE) of the champion EtOH and EtOH/DMF devices.

Sample	J_{SC} (mA/cm^2)	V_{OC} (V)	FF (%)	PCE (%)
EtOH-Reverse	25.47	1.174	79.09	23.7
EtOH-Forward	25.30	1.183	80.90	24.2
EtOH/DMF-Reverse	25.42	1.172	83.00	24.7
EtOH/DMF-Forward	25.52	1.181	82.90	25.0

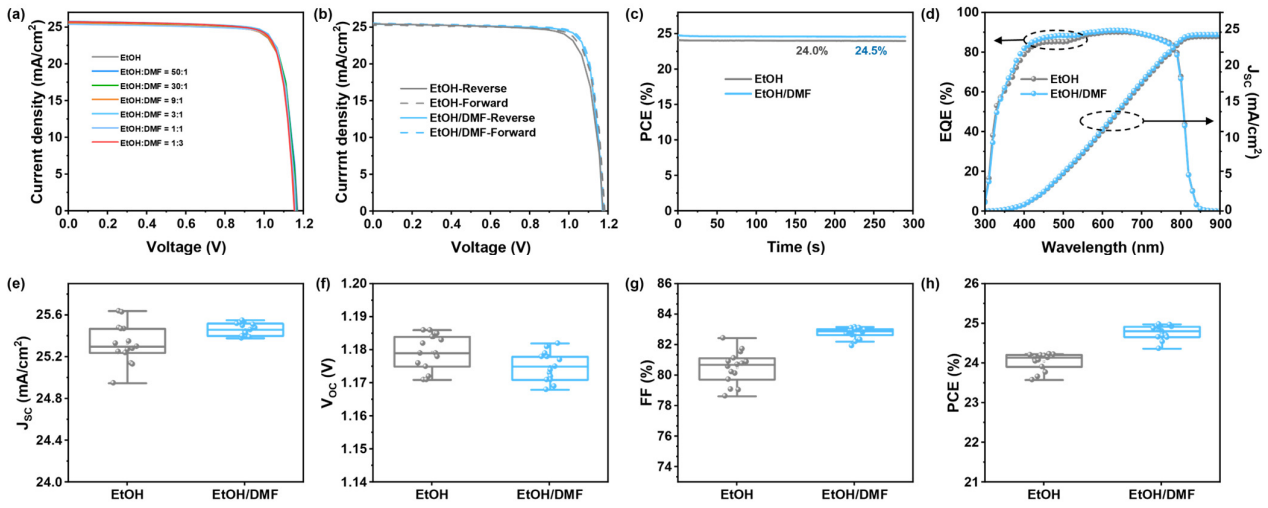

Figure 6. (**a**) *J-V* curves of devices fabricated with SAM solutions at different EtOH/DMF volume ratios; (**b**) Forward and reverse scan *J-V* curves of champion EtOH and EtOH/DMF devices; (**c**) Steady-state power output curves of EtOH and EtOH/DMF devices; (**d**) EQE spectra of EtOH and EtOH/DMF devices. Box plots of the primary photovoltaic parameters of the EtOH and EtOH/DMF devices (**e**) J_{SC}; (**f**) V_{OC}; (**g**) FF; (**h**) PCE.

To demonstrate the enhanced reproducibility of the inverted PSC devices upon adopting the solvent engineering strategy, box plots of the primary photovoltaic parameters of the EtOH and EtOH/DMF devices based on 15 devices for each condition are presented in Figure 6e–h, and the average photovoltaic parameters of the corresponding devices are shown in Table 5. In comparison with the EtOH-only devices, the EtOH/DMF devices exhibit a general enhancement in the device performance with reduced deviation among

individual devices. Such contrast clearly demonstrates that a homogeneous SAM layer via a solvent engineering strategy can efficiently facilitate reproducible fabrication of high-efficiency inverted PSC devices. It is noteworthy that the EtOH/DMF devices generally exhibit lower V_{OC} compared to the EtOH devices, which is likely attributed to the introduction of DMF in the solvent system. The DMF molecule can compete with Me-4PACz for available adsorption and anchoring sites on the ITO surface, which may lead to slightly decreased Me-4PACz bonded onto the ITO surface [28]. Nevertheless, the fill factor is significantly increased due to the optimized SAM layer and perovskite buried interface, which contributes to the improvement of the overall device performance. Finally, the shelf stability of EtOH and EtOH/DMF devices was tested by storing the unencapsulated devices in ambient conditions (25 ± 5 °C, 30% RH) without exposure to light illumination. As shown in Figure 7, the EtOH/DMF device can still retain 90% of its initial PCE after 1152 h of storage in the ambient dark condition, exhibiting superior stability compared with the EtOH device.

Table 5. Average photovoltaic parameters including the short-circuit current density (J_{SC}), open-circuit voltage (V_{OC}), fill factor (FF), and power conversion efficiency (PCE) of 15 devices for EtOH and EtOH/DMF conditions, respectively.

Sample	J_{SC} (mA/cm^2)	V_{OC} (V)	FF (%)	PCE (%)
EtOH	25.33 ± 0.19	1.179 ± 0.005	80.51 ± 1.06	24.0 ± 0.2
EtOH/DMF	25.46 ± 0.06	1.175 ± 0.004	82.78 ± 0.36	24.8 ± 0.1

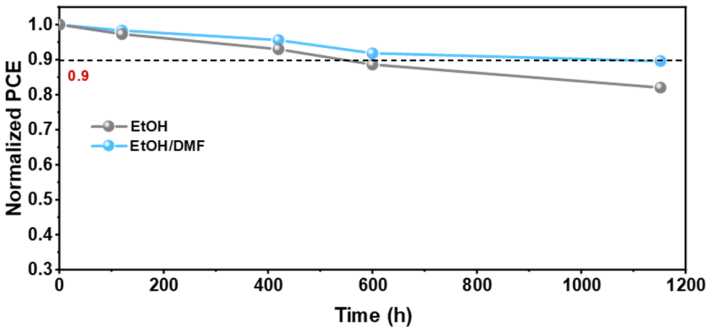

Figure 7. Shelf stability of EtOH and EtOH/DMF devices tested under ambient dark conditions.

4. Discussion

Aiming to achieve deposition of high-quality, homogeneous SAM layers in ambient conditions, this study systematically investigated the feasibility of various common solvents for Me-4PACz solution. The experimental results demonstrate that protic polar solvents readily lead to moisture-driven micron-size aggregation in the resultant SAM layer, whereas aprotic polar solvents with strong dipole characteristics can effectively suppress intermolecular aggregation in the Me-4PACz solution. Inspired by these findings, a mixed-solvent system of EtOH:DMF = 3:1 (volume ratio) is adopted for the Me-4PACz solution. The solvent engineering strategy simultaneously addressed the intermolecular aggregation and the detrimental effect of ambient moisture, leading to a homogeneous SAM-based HTL with subsequently optimized perovskite buried interface. Inverted PSC devices with the optimized SAM-based HTL deliver a considerably increased PCE up to 25.0%. This work provides a feasible strategy for ambient fabrication of SAM-based HTLs, promoting the scalable fabrication of high-efficiency inverted PSCs.

Author Contributions: Conceptualization, X.S. and F.L.; methodology, X.S. and C.W.; validation, F.L. and G.S.; formal analysis, X.S. and C.W.; data curation, G.S. and L.L.; writing—original draft preparation, X.S. and L.L.; writing—review and editing, F.L. and C.W.; visualization, F.L. and C.W.; supervision, Y.Z. and F.L. All authors have read and agreed to the published version of the manuscript.

Funding: This work was supported by the National Natural Science Foundation of China (62304068).

Data Availability Statement: The data presented in this study are available upon request from the corresponding author.

Conflicts of Interest: The authors declare no conflicts of interest.

References

1. Liu, S.W.; Miao, T.Y.; Wang, J.N.; Zhang, Y.; Chen, R.; Lei, X.; Qin, W.; Zhu, Z.; Lu, L.; Chen, Z.; et al. Solvated-intermediate-driven surface transformation of lead halide perovskites. *Nat. Energy* **2026**, *11*, 109–120.
2. Zheng, X.P.; Chen, B.; Dai, J.; Fang, Y.J.; Bai, Y.; Lin, Y.Z.; Wei, H.T.; Zeng, X.C.; Huang, J.S. Defect passivation in hybrid perovskite solar cells using quaternary ammonium halide anions and cations. *Nat. Energy* **2017**, *2*, 17102. [CrossRef]
3. Wang, Y.H.; Zhang, M.N.; Zhang, M.; Liu, X.; Lee, M.W.; Feng, Z.Y.; Yuan, X.J.; Liu, Z.H.; Yun, J.S.; Xu, J.T. A complementary hole-transport layer of PTAA and SAM on FTO substrate for p-i-n structured perovskite solar cells. *Adv. Funct. Mater.* **2026**, *36*, e08510.
4. Jeng, J.-Y.; Chiang, Y.-F.; Lee, M.-H.; Peng, S.-R.; Guo, T.-F.; Chen, P.; Wen, T.-C. $CH_3NH_3PbI_3$ perovskite/fullerene planar-heterojunction hybrid solar cells. *Adv. Mater.* **2013**, *25*, 3727–3732. [CrossRef] [PubMed]
5. Serpetzoglou, E.; Konidakis, I.; Kakavelakis, G.; Maksudov, T.; Kymakis, E.; Stratakis, E. Improved carrier transport in perovskite solar cells probed by femtosecond transient absorption spectroscopy. *ACS Appl. Mater. Interfaces* **2017**, *9*, 43910–43919. [CrossRef] [PubMed]
6. Magomedov, A.; Al Ashouri, A.; Kasparavičius, E.; Strazdaite, S.; Niaura, G.; Jošt, M.; Malinauskas, T.; Albrecht, S.; Getautis, V. Self-assembled hole transporting monolayer for highly efficient perovskite solar cells. *Adv. Energy Mater.* **2018**, *8*, 1801892. [CrossRef]
7. Castriotta, L.A. Entering the 27% era: Practical design rules for single-junction perovskite solar cells. *ACS Energy Lett.* **2026**, *11*, 2378–2381. [CrossRef] [PubMed]
8. Tan, Q.; Li, Z.N.; Luo, G.F.; Zhang, X.; Che, B.; Chen, G.; Gao, H.; He, D.; Ma, G.; Wang, J.; et al. Inverted perovskite solar cells using dimethylacridine-based dopants. *Nature* **2023**, *620*, 545–551. [CrossRef] [PubMed]
9. Xiong, Z.; Zhang, Q.; Cai, K.; Zhou, H.T.; Song, Q.; Han, Z.; Kang, S.; Li, Y.; Jiang, Q.; Zhang, X.; et al. Homogenized chlorine distribution for > 27% power conversion efficiency in perovskite solar cells. *Science* **2025**, *390*, 638–642. [CrossRef] [PubMed]
10. Garg, N.; Carrasquillo-Molina, E.; Lee, T.R. Self-assembled monolayers composed of aromatic thiols on gold: Structural characterization and thermal stability in solution. *Langmuir* **2002**, *18*, 2717–2726. [CrossRef]
11. Isikgor, F.H.; Zhumagali, S.; Merino, L.V.T.; De Bastiani, M.; McCulloch, I.; De Wolf, S. Molecular engineering of contact interfaces for high-performance perovskite solar cells. *Nat. Rev. Mater.* **2023**, *8*, 89–108.
12. Shao, C.; Chen, J.D.; Ma, J.X.; Cui, C.; Nie, Z.X.; Zhang, W.F.; Wang, L.P.; Yu, G.; Wang, J.Z. Rationally designed self-assembled monolayer for dual-site passivation enables efficient and stable perovskite solar cells. *Adv. Mater.* **2026**, *38*, e23249. [CrossRef] [PubMed]
13. Liu, S.W.; Li, J.B.; Xiao, W.S.; Chen, R.; Sun, Z.; Zhang, Y.; Lei, X.; Hu, S.; Kober-Czerny, M.; Wang, J. Buried interface molecular hybrid for inverted perovskite solar cells. *Nature* **2024**, *632*, 536–542. [CrossRef] [PubMed]
14. Sahli, F.; Werner, J.; Kamino, B.A.; Bräuninger, M.; Monnard, R.; Paviet-Salomon, B.; Barraud, L.; Ding, L.; Diaz Leon, J.J.; Sacchetto, D.; et al. Fully textured monolithic perovskite/silicon tandem solar cells with 25.2% power conversion efficiency. *Nat. Mater.* **2018**, *17*, 820–826. [CrossRef] [PubMed]
15. Yu, S.Q.; Xiong, Z.; Zhou, H.T.; Zhang, Q.; Wang, Z.; Ma, F.; Qu, Z.; Zhao, Y.; Chu, X.; Zhang, X. Homogenized NiOx nanoparticles for improved hole transport in inverted perovskite solar cells. *Science* **2023**, *382*, 1399–1404. [CrossRef] [PubMed]
16. Park, S.M.; Wei, M.Y.; Lempesis, N.; Yu, W.; Hossain, T.; Agosta, L.; Carnevali, V.; Atapattu, H.R.; Serles, P.; Eickemeyer, F.T.; et al. Low-loss contacts on textured substrates for inverted perovskite solar cells. *Nature* **2023**, *624*, 289–294. [CrossRef] [PubMed]
17. Yang, Y.Q.; Shi, X.Q.; Stein, A.N.; Lockett, M.R.; Huang, J.S. Understanding phosphonic-acid molecules based hole transport layers in perovskite solar cells. *Adv. Energy Mater.* **2026**, *16*, e05937.
18. Li, Z.; Sun, X.L.; Zheng, X.P.; Li, B.; Gao, D.; Zhang, S.; Wu, X.; Li, S.; Gong, J.; Luther, J.M. Stabilized hole-selective layer for high-performance inverted pin perovskite solar cells. *Science* **2023**, *382*, 284–289. [CrossRef] [PubMed]
19. Chen, B.; He, X.P.; Yu, J.Y.; He, Z.; Peng, C.; Zhang, F.; Guo, R.; Wang, L. Hybrid self-assembled molecules reduce interfacial defects in perovskite light-emitting diodes. *ACS Energy Lett.* **2025**, *10*, 4013–4018. [CrossRef]

20. Li, D.Y.; Lian, Q.; Du, T.; Ma, R.J.; Liu, H.; Liang, Q.; Han, Y.; Mi, G.; Peng, O.; Zhang, G.; et al. Co-adsorbed self-assembled monolayer enables high-performance perovskite and organic solar cells. *Nat. Commun.* **2024**, *15*, 7605. [CrossRef] [PubMed]
21. Liu, T.Q.; Liao, X.C.; Wu, J.; Ding, P.; Shao, Z.; Sun, H.; Li, J.; Yang, D.; Ge, Z. Dimeric self-assembled molecules modulate phase homogeneity and anchoring stability for high-performance perovskite solar cells. *Adv. Funct. Mater.* **2026**, *36*, e20189.
22. Zhao, C.Y.; Wang, F.F.; Hu, X.D.; Zhang, Y.; Liu, T.; Liu, Y.; Wang, L.; Luo, S.; Shi, X.; Tang, X.; et al. Ambient blade-coated perovskite solar cells with high reverse bias stability enabled by polymeric hole transporter design. *Nat. Commun.* **2025**, *16*, 10355. [CrossRef] [PubMed]
23. Lin, Y.H.; Vikram; Yang, F.N.; Cao, X.L.; Dasgupta, A.; Oliver, R.D.J.; Ulatowski, A.M.; McCarthy, M.M.; Shen, X.; Yuan, Q.; et al. Bandgap-universal passivation enables stable perovskite solar cells with low photovoltage loss. *Science* **2024**, *384*, 767–775. [CrossRef] [PubMed]
24. Zhao, H.Y.; Zhang, X.W.; Zhang, K.; Zhang, W.F.; Zhou, R.; Wei, Y.B.; Qu, J.; Chen, Y.D.; Li, H.Y.; Zong, X.P.; et al. Synergistic self-assembled monolayers reinforce buried interface anchoring for high-efficiency tandem perovskite solar cells. *Angew. Chem. Int. Ed.* **2025**, *64*, e202504237. [CrossRef]
25. Lide, D.R. (Ed.) *CRC Handbook of Chemistry and Physics*, 85th ed.; CRC Press LLC: Boca Raton, FL, USA, 2004.
26. Bautista-Quijano, J.R.; Telschow, O.; Paulus, F.; Vaynzof, Y. Solvent–antisolvent interactions in metal halide perovskites. *Chem. Commun.* **2023**, *59*, 10588–10603. [CrossRef]
27. Du, G.X.; Jiang, W.L.; Zhang, N.; Wang, Y.; Liu, M.; Lei, T.; An, Y.; Ke, L.; Ge, C.; Lin, F.R.; et al. Efficient organic solar cells with a printed p-i-n stack enabled by an azeotrope-processed self-assembled monolayer. *Energy Environ. Sci.* **2025**, *18*, 799–806. [CrossRef]
28. Ying, Z.Q.; Su, S.Q.; Li, X.; Chen, G.; Lian, C.; Lu, D.; Zhang, M.; Guo, X.; Tian, H.; Sun, Y.; et al. Antisolvent seeding of self-assembled monolayers for flexible monolithic perovskite/Cu(In,Ga)Se_2 tandem solar cells. *Nat. Energy* **2025**, *10*, 737–749. [CrossRef]
29. Cao, H.; Dou, M.Y.; Lyu, Z.X.; Wang, Y.; Pedersen, C.M.; Qiao, Y. Understanding the interaction mechanism of carbazole/anthracene with N,N-dimethylformamide: NMR study substantiated carbazole separation. *Ind. Chem. Mater.* **2023**, *1*, 240–246. [CrossRef]
30. Aydin, E.; Ugur, E.; Yildirim, B.K.; Allen, T.G.; Dally, P.; Razzaq, A.; Cao, F.; Xu, L.; Vishal, B.; Yazmaciyan, A.; et al. Enhanced optoelectronic coupling for perovskite/silicon tandem solar cells. *Nature* **2023**, *623*, 732–738. [CrossRef] [PubMed]
31. Zhang, J.; Gan, N.; Liu, F.; Xie, X.; Zhang, X.; Wu, C.; Shi, D.; Xu, T.; Cai, S.; Guo, H.; et al. Revealing performance-limiting buried interfaces in layered Dion–Jacobson lead–iodide perovskites. *J. Am. Chem. Soc.* **2025**, *147*, 30873−30884. [CrossRef]
32. Zhang, X.W.; Wang, Y.; Zhang, K.; Tao, M.; Guo, H.; Guo, L.; Song, Z.; Wen, J.; Yang, Y.; Hou, Y. Reinforcing coverage of self-assembled monomolecular layers for inverted perovskite solar cells with efficiency of 25.70%. *Angew. Chem. Int. Ed.* **2025**, *64*, e202423827. [CrossRef]
33. Chen, B.; Rudd, P.N.; Yang, S.; Yuan, Y.B.; Huang, J.S. Imperfections and their passivation in halide perovskite solar cells. *Chem. Soc. Rev.* **2019**, *48*, 3842–3867. [CrossRef] [PubMed]
34. Péan, E.V.; Dimitrov, S.; De Castroc, C.S.; Davies, M.L. Interpreting time-resolved photoluminescence of perovskite materials. *Phys. Chem. Chem. Phys.* **2020**, *22*, 28345–28358. [CrossRef] [PubMed]
35. Keeble, D.J.; Wiktor, J.; Pathak, S.K.; Phillips, L.J.; Dickmann, M.; Durose, K.; Snaith, H.J.; Egger, W. Identification of lead vacancy defects in lead halide perovskites. *Nat. Commun.* **2021**, *12*, 5566. [CrossRef] [PubMed]